

*XMM-Newton* **Detection of a Compton-thick AGN in the 1-Jy  
ULIRG/LINER F04103–2838**

Stacy H. Teng,<sup>1</sup> S. Veilleux, A. S. Wilson

*Department of Astronomy, University of Maryland, College Park, MD 20742*

A. J. Young

*Center for Space Research, Massachusetts Institute of Technology, Cambridge, MA 02139*

D. B. Sanders

*Institute for Astronomy, University of Hawaii, 2680 Woodlawn Drive, Honolulu, HI 96822*

and

N. M. Nagar

*Astronomy Group, Departamento de Física, Universidad de Concepción, Casilla 160-C,  
Concepción, Chile*

**ABSTRACT**

We report on the detection of Fe K $\alpha$  emission in F04103–2838, an ultraluminous infrared galaxy (ULIRG;  $\log[L_{\text{IR}}/L_{\odot}] \geq 12$ ) that is optically classified as a LINER. Previous *Chandra* observations suggested the presence of both a starburst and an AGN in this source. A deeper ( $\sim 20$  ksec) *XMM-Newton* spectrum reveals an Fe K $\alpha$  line at rest frame energy  $\sim 6.4$  keV, consistent with cold neutral iron. The best-fit spectral model indicates the Fe K $\alpha$  line has an equivalent width of  $\sim 1.6$  keV. The hard X-ray emission is dominated by a Compton-thick AGN with intrinsic 0.2–10 keV luminosity  $\sim 10^{44}$  ergs s $^{-1}$ , while the soft X-ray emission is from  $\sim 0.1$  keV gas attributed to the starburst. The X-ray spectrum of this source bears a striking resemblance to that of the archetypal luminous infrared galaxy NGC 6240 despite differences in merger state and infrared properties.

*Subject headings:* galaxies: active — galaxies: starburst — galaxies: individual: F04103–2838 — X-rays: galaxies

---

<sup>1</sup>Contacting author: stacyt@astro.umd.edu

## 1. Introduction

The primary energy source (AGN versus starburst activity) of ultraluminous infrared galaxies (ULIRGs;  $\log[L_{\text{IR}}/L_{\odot}] \geq 12$ ) is still a matter of debate. Optical and infrared emission-line spectra suggest that the energy output of most local ULIRGs is dominated by starbursts, but the “warm” infrared colors and quasar-like spectra of the more luminous ULIRGs indicates that black-hole driven activity plays an increasingly important role in these objects (e.g., Veilleux et al. 1995, 1997, 1999a, 1999b; Genzel et al. 1998; Surace & Sanders 1999; Tran et al. 2001). The dusty, gas-rich nature of ULIRGs implies, however, that observations in energy bands other than radio and X-ray may not always probe the true nuclear energy source of these objects. Since the luminosity of ULIRGs in the radio is insignificant, X-ray observations remain arguably the best option to solve this energy source mystery.

Unresolved hard X-ray emission is in principle a telltale sign of a dominant AGN. However, if a large column density of gas ( $\gtrsim 10^{24} \text{ cm}^{-2}$ ) is located in front of the nucleus, then directly viewed X-rays from the AGN will be strongly attenuated. For such cases, Fe K $\alpha$  lines with large equivalent widths ( $\gtrsim 1 \text{ keV}$ ) are expected due to scattering off circumnuclear material (e.g., Ghisellini et al. 1994; Krolik 1994). Thus, the discovery of such Fe K $\alpha$  lines may be the best evidence for energetically dominant AGNs in highly obscured ULIRGs.

In recent years, three X-ray surveys have added considerably to our knowledge of ULIRGs. Ptak et al. (2003) performed a volume-limited ( $z < 0.045$ ) survey of ULIRGs with *Chandra*. On the basis of their dust temperatures (25-to-60  $\mu\text{m}$  flux ratio) and X-ray luminosities, three of the eight ULIRGs sampled by Ptak et al. (2003) were classified as AGN-dominated (Mrk 231, Mrk 273, and F05189-2524). In the same year, Franceschini et al. (2003) published the results of a similar survey with *XMM-Newton* that focused on the brightest local ULIRGs (only one ULIRG in their sample had  $z > 0.082$ ). Of the ten ULIRGs sampled by Franceschini et al. (2003), three were AGN-dominated (Mrk 231, F19254-7245, and F20551-4250) and two had X-ray signatures of both a starburst and an AGN (F20100-4156 and F23128-5919). All of the AGN-dominated ULIRGs showed strong Fe K emission lines (Maloney & Reynolds 2000; Braito et al. 2003; Ptak et al. 2003; Franceschini et al. 2003; Braito et al. 2004). These two pioneering surveys proved the viability of using the X-ray emission as a diagnostic for AGN activity in ULIRGs. However, these two surveys only studied a small set of the nearest and brightest ULIRGs, and therefore were not able to draw general conclusions on the issue of the energy source among ULIRGs as a class.

In an attempt to expand this type of study to a more characteristic sample of ULIRGs, our group (Teng et al. 2005, hereafter Paper I) conducted a snapshot (10 ksec/target) survey

of 14 ULIRGs from the 1-Jy sample<sup>2</sup>. These sources were carefully selected to sample the full range of infrared luminosities and infrared colors that characterize the entire class of local ULIRGs. All 14 galaxies were detected by *Chandra*, though most (11/14) had less than 40 counts. The analysis showed that the two brightest galaxies in the sample have optical and X-ray spectral characteristics of Seyfert 1 nuclei. Most others have X-ray photon indices (estimated using hardness ratios) and hard X-ray to far-infrared flux ratios which are similar to those of starbursts.

One exception, F04103–2838, had a hardness ratio (deduced from only 30 counts) that suggested the presence of a starburst coexisting with an AGN. The low signal-to-noise data could not distinguish between a Compton-thick AGN or an intrinsically faint nuclear source. This object is optically classified as a LINER (Veilleux et al. 1999a). F04103–2838 has one of the largest 25-to-60  $\mu\text{m}$  flux ratios of all 1 Jy ULIRGs ( $f_{25}/f_{60} = 0.30$ ). In fact, this is the warmest of all *IRAS* 1 Jy ULIRGs with optical LINER or H II classification. This source is even warmer than some of the Seyfert galaxies in the 1 Jy sample (see Fig. 1 of Paper I). Recent *Spitzer* detection of [Ne V] and [O IV] lines from this source has confirmed the existence of an AGN in this system (Veilleux et al. 2007, in prep.), making it a rare example of a ULIRG optically classified as a LINER that is not classified as a starburst on the basis of mid-infrared spectroscopy (Lutz, Veilleux, & Genzel 1999; Taniguchi et al. 1999). In this paper, we present an *XMM-Newton* observation of F04103–2838 which delves deeper into the nature of this AGN.

F04103–2838 is an interacting galaxy system in the late stages of a merger as indicated by the presence of a single nucleus with distinct tidal tails (Veilleux et al. 2002; Dasyra et al. 2006a). This object has an infrared (8–1000  $\mu\text{m}$ ) luminosity of  $10^{12.15}L_{\odot}$  and a cosmological redshift of 0.118. Assuming  $H_0 = 75 \text{ km s}^{-1} \text{ Mpc}^{-1}$  and  $q_0 = 0$  (used throughout this paper), the luminosity distance of this object is 497 Mpc. At this distance, 1'' corresponds to  $\sim 2.4$  kpc. In §2 of this paper, we describe our new *XMM-Newton* observation of F04103–2838 and the methods we used to reduce these data. In §3, we present the analysis of these data, emphasizing the results on the X-ray morphology, the lack of flux variability, and the spectral decomposition of the X-ray emission. The implications of these results are discussed in §4. The main conclusions are summarized in §5.

---

<sup>2</sup>The 1 Jy sample of ULIRGs is comprised of *IRAS* galaxies with fluxes at 60  $\mu\text{m}$  exceeding 1 Jy,  $L_{\text{IR}} \geq 10^{12} L_{\odot}$ , galactic latitude  $|b| > 30^{\circ}$ ,  $f(60 \mu\text{m}) > f(12 \mu\text{m})$  (to avoid stars), *IRAS* color  $\log[f_{60}/f_{100}] > -0.3$  (to favor luminous infrared systems), and redshift  $0.018 < z < 0.268$  (Kim & Sanders, 1998).

## 2. Observation and Data Reduction

F04103–2838 was observed with *XMM-Newton* during orbit #1132 on 13 February, 2006 (ObsID: 0301330401; PI: Wilson) with the EPIC instrument. The EPIC cameras were operating in full-frame mode. Each of the detectors used the medium filter.

The data were processed using the standard procedures of the *XMM-Newton* Science Analysis System (SAS) version 6.5.0 released on 17 August, 2005. The processing procedures outlined in §4.11 of the *XMM-Newton* SAS User’s Guide were followed. The event lists were calibrated with the latest available calibration files as of June, 2006. Times of high background flares were flagged. The total good time interval on source for each camera was 17.5 ksec for PN, 21.8 ksec for MOS1, and 21.5 ksec for MOS2.

Source and background counts were extracted from circular regions with radii of 24". Because the source is near a gap in the CCD and a nearby X-ray luminous source, the background was extracted from a circular region with the same area as the source extraction region in a neighboring piece of the sky in which no obvious X-ray sources reside. The total 0.2–10 keV counts extracted from the source region are 224 for PN, 52 for MOS1, and 48 from MOS2. The expected background counts in the source region are 45 for PN and 50 for MOS1/2 based on the expected background count rates quoted in the *XMM* User’s Handbook. Since the extracted source counts are approximately the same as the expected background counts for the MOS detectors, we will exclude the MOS spectra in our spectral analysis of the source.

## 3. Analysis

In §3.1, we describe the distribution of the X-ray emission from F04103–2838. In §3.2 we point out the lack of variability of this object. A detailed analysis of the X-ray spectrum and iron complex is presented in §3.3.

### 3.1. Morphology

To improve the signal-to-noise ratio of the images, the PN and MOS1/2 events were combined using the SAS task *emosaic* and then smoothed with a 5" Gaussian using *asmooth* to match the spatial resolution of *XMM*. The resultant image is displayed in the left panel of Figure 1. A comparison of the 0.2–2 keV (unsmoothed) radial profile with the *XMM-Newton* point spread function (PSF) at 1 keV indicates that the source is unresolved (see Fig. 1,

right panel). Only the EPIC PN data were used for the radial profile calculations because of the small number of counts detected by the MOS1/2 cameras. The PSF of the PN camera is well described by a King profile<sup>3</sup> and was normalized so that the total number of counts per square pixel under the curve match the total number of detected counts per square pixel. The *Chandra* data from Paper I verifies that the source is unresolved.

### 3.2. X-Ray Variability

The time interval covered by our observation was divided into four equal bins of 5234 seconds to search for significant X-ray variability, another potential indicator of dominant AGN activity. The 0.2–10 keV and 2–10 keV EPIC PN count rates were calculated for both source and background. Figure 2 shows the 0.2–10 and 2–10 keV light curves of the source and background. To within the errors, the source is not significantly variable on the 5-6 hour time scale of our observations.

### 3.3. X-Ray Spectra

The extracted source and background spectra from each detector were binned using the FTOOL *grppha* to at least 3, 5, and 15 counts bin<sup>-1</sup>. The binned and unbinned spectra were then analyzed using XSPEC version 11.3.2t. The quoted errors on the derived best-fitting model parameters correspond to a 90% confidence level ( $\Delta\chi^2/\Delta\text{c-stat} = 2.706$ ). The  $\chi^2$  goodness-of-fit test was used to judge the fits to the spectrum binned to at least 15 counts bin<sup>-1</sup>. The Cash statistics (c-stat) option in XSPEC was used for spectra binned to at least 3 and 5 counts bin<sup>-1</sup> and the unbinned data. The spectral model was applied to the EPIC PN data only (see §2). All models were corrected for Galactic absorption using  $N_{\text{H,Galactic}} = 2.45 \times 10^{20}$  atoms cm<sup>-2</sup> (Dickey & Lockman 1990).

#### 3.3.1. Effects of Binning

By definition, spectra binned to at least 15 counts bin<sup>-1</sup> have the highest signal-to-noise ratios while the spectra binned to at least 3 counts bin<sup>-1</sup> show the most spectral details. The first task is to determine whether the mode of binning affects the spectral parameters

---

<sup>3</sup>PSF =  $A[1 + (\frac{r}{r_0})^2]^{-\alpha}$ , where  $A \sim 4.756$ ,  $r_0 \sim 5.5$  pixels, and  $\alpha \sim 1.6$  (Kirsch et al. 2006).

derived from the best-fit model<sup>4</sup>. Since Cash-statistics were developed for the modeling of unbinned data, we also modeled the unbinned spectrum for comparison.

Two simple models were applied to the spectra. Model A is an absorbed power-law distribution. Model B is the same as A, except for the inclusion of a Gaussian component to model the Fe K emission at 6–7 keV (rest frame). Table 1 lists the best-fit parameters of each model and Figure 3 shows each set of spectra with the best-fit models. The significant improvement in fitting statistics of model B over model A suggests that there is indeed an emission line at an energy consistent with Fe K $\alpha$  emission. However, since the number of counts is relatively low (especially when the data is binned to only 3 or 5 counts bin<sup>-1</sup>), the F-test cannot be used to determine whether the addition of the Gaussian component to model A is significant. The likelihood of the line being a result of statistical variations was tested using simulations. To this end, 10000 spectra were created using the *fakeit* command in XSPEC for each set of binned or unbinned data. The simulated spectra were created using model A. Then these spectra were fitted by both models A and B. If the line is a result of statistical variations, then one would expect a large fraction of the simulated spectra to be well described by model B. The fitting statistics were used to calculate  $\Delta c\text{-stat}(A-B)$  [or  $\Delta\chi^2(A-B)$  for the 15 counts bin<sup>-1</sup> data] which was then compared with the values presented in Table 1. For the 15 counts bin<sup>-1</sup> data, 1000 of 10000 (10.0%) had  $\Delta\chi^2$  greater than 3.76. This implies that model B (the inclusion of the emission line) is significant at the 90.0% level (a 1.6- $\sigma$  detection). Similarly, the simulations show that the line is significant at the 96.87% level (313 out of 10000; 2.2 $\sigma$ ) for the 5 counts bin<sup>-1</sup> data, at the 93.5% level (507 out of 10000; 1.8 $\sigma$ ) for the 3 counts bin<sup>-1</sup> data, and at the 94.0% level (608 out of 10000; 1.9 $\sigma$ ) for the unbinned data. From these simulations, the line is significant to at least the 90.0% level.

The 3 counts bin<sup>-1</sup> data also suggest that the iron line can be decomposed into two narrower emission lines with centroid energies at 6.3 (EW  $\sim$ 0.6 keV) and 6.7 keV (EW  $\sim$ 0.4 keV) in the rest frame. These energies are consistent with emission arising from neutral

---

<sup>4</sup>Gaussian statistics apply to data binned to at least 15 counts bin<sup>-1</sup> while Poisson statistics apply to the data binned to at least 3 or 5 counts bin<sup>-1</sup> and unbinned data. Since the difference of two Gaussian distributions remains a Gaussian distribution, a background-subtracted spectrum binned to at least 15 counts bin<sup>-1</sup> retains the properties of a Gaussian distribution and can be modeled normally. However, the same is not true for a Poisson distribution. Therefore, the background cannot be simply subtracted for data binned to at least 3 or 5 counts bin<sup>-1</sup> and unbinned data and then modeled. One way of treating the background is to model the background spectrum separately and then add the background model to the continuum model when fitting the source spectrum. For this paper, the background is modeled using a simple, relatively flat power law ( $\Gamma \sim 1.0$ ). This treatment of the background is applied to all modeling of data binned to at least 3 and 5 counts bin<sup>-1</sup> and the unbinned spectrum. A representation of the background spectrum and model is shown in the bottom panel of Figure 4.

iron and Fe XXV, respectively. The fitting statistics of the double-line model to the unbinned data is only slightly better than that of the single-line model. The detection of these narrow lines in the Fe K complex is significant at only the  $\sim 60\%$  level based on 10000 simulations of the unbinned data. Therefore, the detection of the doublet needs to be confirmed with data of higher spectral resolution and signal-to-noise ratio.

Our modeling and simulations show that Cash-statistics give consistent results for the unbinned spectrum and the spectra binned to at least 3 and 5 counts  $\text{bin}^{-1}$ . Since Cash statistics were designed for unbinned spectra, we will use only the unbinned spectrum in subsequent modeling. The iron line is most prominent in the data binned to at least 5 counts  $\text{bin}^{-1}$ , we will use the spectrum binned to at least 5 counts  $\text{bin}^{-1}$  as a visual and qualitative check for the model of the unbinned data.

### 3.3.2. AGN + Starburst Continuum Models

Aside from models A and B mentioned above, we modeled the unbinned spectrum with slightly more complex models to account for the possibility that a starburst may coexist with the AGN in F04103–2838. Cautioning against over-interpreting data with only modest signal-to-noise ratios, even these more “complex” models were kept as simple as possible.

The first model (model C) is a combination of absorbed power-law and MEKAL spectra (with metallicity fixed at solar) representing the emission from the AGN and starburst, respectively. The second model (model D) is a combination of two absorbed power laws, with one power law representing the AGN and the other representing the high mass X-ray binaries (HMXBs) associated with the possible starburst in this object. Finally, a third model (model E) was a combination of the two above mentioned models: a power law for the AGN, a power law for the HMXBs, and a MEKAL model for the hot gas. For all of these models, a Gaussian with centroid energy between 6 and 7 keV was included to model the iron line.

While all of these models give better fitting statistics than the simpler power law models, only model C is a realistic fit to the data. Models D and E are rejected on the grounds that the best-fit power law values are physically unrealistic descriptions of AGNs. Therefore, we adopt model C as the “best-fit model” (Figure 4) and list the fitting parameters in Table 1. This is perhaps not surprising given that ULIRGs are known from observations at optical and infrared wavelengths to show the presence of both an AGN and a starburst (e.g., Genzel et al. 1998; Kim, Veilleux, & Sanders 1998); F04103–2838 does not appear to be an exception.

## 4. Discussion

### 4.1. The Soft Component

The results from the spectral fitting suggest that the soft X-ray (0.2–2 keV) flux is best described as thermal emission from hot gas with  $kT \sim 0.1$  keV ( $T \sim 1.2 \times 10^6$  K). This is somewhat lower than the range of gas temperatures (0.6–0.8 keV) found in LINERs (González-Martín et al. 2006). The results for F04103–2838 is also somewhat lower than the results from Grimes et al. (2005) who performed a *Chandra* archival study of the soft X-ray emission from starburst galaxies ranging in luminosity from dwarf galaxies to ULIRGs. The authors found that the soft X-ray thermal emission of these starburst galaxies tends to fall in the temperature range  $kT \sim 0.25$ –0.8 keV with ULIRGs occupying the upper end of this temperature range. These large temperatures can all be attributed to powerful starbursts.

The soft X-ray emission in F04103–2838 is likely the result of thermal bremsstrahlung from a hot gas produced by the merger-induced starburst or by intrinsically extended soft X-ray emission heated by the AGN. If the ion density equals that of the electrons, the relationship between the electron density ( $n_e$ ) and luminosity of an emitting region of a given volume ( $V$ ) is

$$L_{ff} \approx 1.7 \times 10^{-25} n_e^2 f V \text{ ergs s}^{-1}, \quad (1)$$

where  $f$  is the filling factor for the hot gas<sup>5</sup>. The non-AGN contribution of the nominal 0.2–2 keV luminosity from the best-fit model (model C) for F04103–2838 is  $1.6 \times 10^{41}$  ergs s<sup>-1</sup>. Assuming the emitting region is spherical with a diameter of  $\leq 5''$ <sup>6</sup>, the average electron density has a lower limit of  $\sim 0.19 f^{-1/2}$  cm<sup>-3</sup>. This value is consistent with simulation results for the warm ( $10^{5.5} \lesssim T \lesssim 10^{6.5}$  K) component in the wind models of Strickland & Stevens (2000).

Observationally, this hot gas component is difficult to probe because of its low density and emissivity. Strickland & Stevens (2000) performed hydrodynamic simulations of starburst-driven galactic winds with various ISM models. The authors found that, in general, the soft X-ray emission comes from gas with low filling factors ( $10^{-3} < f < 10^{-1}$ ; see also Cecil, Bland-Hawthorn, & Veilleux 2002; and Strickland et al. 2004a, 2004b for

---

<sup>5</sup>Equation 1 is based on equation (5.14b) and Figure 5.2 of Rybicki & Lightman (1979) for  $T = 10^6$  K in the energy range of 0.2–2 keV.

<sup>6</sup>While the selection of a  $\leq 5''$  emitting region is based on the spatial resolution of the telescope, it should be noted that the linear diameter of  $5''$  at the distance of F04103–2838 is less than a factor of two larger than the soft X-ray (0.5–2.5 keV) emitting region of NGC 6240 (Komossa et al. 2003). Therefore, the assumption of a  $\leq 5''$  diameter is reasonable, even though it was chosen based on the instrument PSF.



observational constraints). Using these values for  $f$ , the electron density of the hot gas in F04103–2838 is  $\sim 0.6\text{--}5.9\text{ cm}^{-3}$ , consistent with values derived by Netzer et al. (2005) in NGC 6240.

The soft X-ray emission detected in F04103–2838 may be thus the result of superwinds from the starburst. X-ray superbubbles have been observed in Arp 220 (Iwasawa et al. 2005) and NGC 6240 (Netzer et al. 2005). Furthermore, powerful outflow events are now thought to take place in most ULIRGs (e.g., Rupke et al. 2002, 2005a, b, c, though their sample did not include F04103–2838).

## 4.2. The Iron Feature

F04103–2838 joins the growing list of ULIRGs with Fe K detections [e.g. Arp 220 (Iwasawa et al. 2005), Z11598-0112 (Paper I), F19254-7245 (Franceschini et al. 2003; Braito et al. 2003), Mrk 231 (Maloney & Reynolds 2000; Ptak et al. 2003; Braito et al. 2004), F05189-2524 (Ptak et al. 2003), Mrk 273 (Ptak et al. 2003), and UGC 05101 (Imanishi et al. 2003; Ptak et al. 2003)], supporting the view that an obscured AGN exists in many of these objects. The presence of an AGN in F04103–2838 was first suggested by Paper I based on the large hard X-ray to far-infrared flux ratio; the *XMM* detection of Fe K now indicates that the luminosity of this AGN has probably been underestimated.

Few LINERs have detected Fe  $K\alpha$  lines. Terashima et al. (2002) studied a sample of 53 LINERs and low-luminosity Seyfert galaxies using *ASCA*. Of the 21 LINERs in their sample, Fe emission lines were detected in only five galaxies (NGC 1052, NGC 3998, NGC 4261, NGC 4579, and NGC 4736). Of these five objects, only four (i.e. those excluding NGC 4261) have centroid line energies consistent within the uncertainties of the measurements with Fe  $K\alpha$  emission due to neutral iron ( $E \sim 6.4\text{ keV}$ ).

Three other LINERs have known Fe K detections; all three are powerful luminous or ultraluminous infrared galaxies. These galaxies are Arp 220 (Iwasawa et al. 2005), NGC 6240 (Ptak et al. 2003; Komossa et al. 2003), and UGC 5101 (Imanishi et al. 2003; Ptak et al. 2003). *Chandra* observations of Arp 220, the archetypal ULIRG, show an iron line at  $6.7\pm 0.1\text{ keV}$ . This is consistent with emission due to Fe XX up to Fe XXVI, but not neutral iron at 6.4 keV (Iwasawa et al. 2005). Komossa et al. (2003) detected Fe K emission from each of the two nuclei in NGC 6240. Their analysis showed that the iron lines in each nucleus are consistent with Fe  $K\alpha$  and Fe  $K\beta$  emissions.

In Figure 5 we show the distribution of published Fe K equivalent widths of all LINERs and ULIRGs known to have line emission. Arp 220, NGC 6240, and F04103–2838

appear to have iron emission with the greatest EW measurements of all the LINERs and ULIRGs. These large Fe K features could be results of the blending of multiple narrower lines. Komossa et al. (2003) did not publish the EWs of the lines from each of the nuclei in NGC 6240. The result quoted here is from Ptak et al. (2003). The authors did not distinguish Fe  $K\alpha$  emission from Fe  $K\beta$  emission and the EW measurement is likely dominated by the brighter southern nucleus alone. The large equivalent widths of the ULIRGs are telltale signs of obscured AGNs where line-of-sight columns of material exceeding  $10^{24}$   $\text{cm}^{-2}$  prevent a direct view of the AGN; the 2 – 10 keV flux is dominated by light scattered off dust or electrons (e.g., Ghisellini et al. 1994; Krolik et al. 1994). The large amount of molecular gas ( $\sim 10^4 M_{\odot} \text{pc}^{-2}$ ) within 400 pc from the nuclei of NGC 6240 (e.g., Bryant & Scoville 1999) is sufficient to cause this obscuration. A similar explanation likely applies to F04103–2838, although we are not aware of any CO measurements in this system.

Interestingly, the Fe K complex in NGC 6240 breaks up into a number of narrow lines. Both Netzer et al. (2005) and Boller et al. (2003) detected Fe K lines due to neutral iron ( $6.41 \pm 0.2$  keV), Fe XXV ( $6.68 \pm 0.02$  keV), and Fe XXVI ( $7.01 \pm 0.04$  keV) in NGC 6240. Komossa et al. (2003) also detected lines at 6.4 and 6.95 keV. The centroid energies of the lines due to neutral iron and Fe XXV in NGC 6240 are consistent with the respective centroid energies suggested by the doublet in the F04103–2838 3 counts  $\text{bin}^{-1}$  data. Although simulations suggest the two line model is only significant at the  $\sim 60\%$  level, a FWHM of  $\sim 30000$   $\text{km s}^{-1}$  ( $\sigma \sim 0.3$  keV) seems too broad and the two component interpretation may be more likely. The Fe XXVI line in NGC 6240 is much fainter than the other lines so it is not surprising that we were unable to detect this feature in the modest signal-to-noise ratio data of F04103–2838.

Despite their X-ray similarities, F04103–2838 is  $\sim 2.5$  times more infrared luminous than NGC 6240. These objects also differ in terms of *IRAS*  $f_{25}/f_{60}$  ratios (0.15 for NGC 6240 and 0.30 for F04103–2838) and merger state (NGC 6240 is in a pre-merger phase with a nuclear separation of  $\sim 1.3$  kpc while F04103–2838 is in the post-merger stage with a single coalesced nucleus). There is growing observational evidence (e.g., Veilleux et al. 2002, 2006; Ishida 2004; Dasyra et al. 2006a, b, 2007) and theoretical motivation (e.g., Hopkins et al. 2005) that mergers of gas-rich galaxies often produce “cool” ( $f_{25}/f_{60} < 0.2$ ) luminous infrared galaxies that evolve into “warm” ( $f_{25}/f_{60} \geq 0.2$ ) ULIRGs before becoming optical quasars. If this evolutionary sequence applies to NGC 6240 and F04103–2838, the first object may actually be the precursor to the latter.

### 4.3. Energy Source of the ULIRG

The lack of short timescale variability (see §3.2) is to be expected if most of the primary X-ray flux is being absorbed or reprocessed. As discussed in §4.2, the large equivalent width of the iron line in F04103–2838 implies the presence of a highly obscured AGN. It is very difficult in such cases to estimate the intrinsic luminosity of the AGN without measurements of the  $> 10$  keV flux from the buried AGN (e.g., Mrk 231; Braito et al. 2004). Here we follow the method of Maloney & Reynolds (2000) to estimate the intrinsic luminosity of F04103–2838.

In their analysis of an *ASCA* observation of Mrk 231, they discussed two ways of estimating the intrinsic AGN flux. The observed X-ray flux is due to a combination of two effects: reflection and scattering. Maloney & Reynolds (2000) estimated the intrinsic AGN flux from the reflection and the scattering components separately. In their geometry, the observer has an obstructed view of the nucleus so the observed flux must be either scattered or reflected into the line of sight along which there is some amount of absorbing material. The reflected component is light from the central engine reflected off of the circumnuclear torus; the amount of reflection depends on the size of the reflecting surface and the composition of the torus. On the other hand, the scattered component is light from the central engine (unobstructed by the torus) scattered into the line of sight. Based on their spectral fitting of the *ASCA* data, Maloney & Reynolds (2000) found that the X-ray flux of Mrk 231 is scattering-dominated with 75% scattered and 25% reflected light.

Due to the low signal-to-noise ratio of our data on F04103–2838, the same spectral fitting as performed by Maloney & Reynolds (2000) could not be done. The large equivalent width of the Fe  $K\alpha$  line ( $\sim 1.6$  keV) above 1 keV suggests a reflection-dominated spectrum. However, the width of the line implies it could be a blend of narrower Fe  $K\alpha$  and ionized iron emission lines (as suggested by the 3 counts  $\text{bin}^{-1}$  data). If this were the case, the Fe  $K\alpha$  EW may be more consistent with a scattering dominated spectrum. Therefore, we will consider two cases: (1) the majority of the observed flux is due to reflection and (2) the majority of the observed flux is due to scattering to estimate the intrinsic X-ray luminosity of the AGN.

After correction for absorption, the nominal 0.2–10 keV flux of the buried AGN in F04103–2838 derived from our best-fit model (model C) is  $1.83 \times 10^{42}$  ergs  $\text{s}^{-1}$ . In the first scenario, we will assume the reflection component is 75% and the scattering component is 25% of the total observed flux. This implies that  $L_{\text{scattered}} = 0.45 \times 10^{42}$  ergs  $\text{s}^{-1}$  and  $L_{\text{reflected}} = 1.38 \times 10^{42}$  ergs  $\text{s}^{-1}$  for the AGN in F04103–2838. In Maloney & Reynolds (2000), the luminosity from the reflected portion is scaled up by a factor of 25 in their modeling of the reflection process. The reflection process differs for different galaxies; it depends on the

ionization state of the mirror and the steepness of the photon index of the central black hole. Maloney & Reynolds (2000) assumed reflection from neutral material, a reflecting fraction of 10%, and the canonical value of the photon index due to an AGN ( $\Gamma = 1.8$ ). The scaling factor used by Maloney & Reynolds (2000) corrects for the flattening of a spectrum with  $\Gamma = 1.8$  to  $\Gamma \sim 1.1$  (based on a single absorbed power-law model) for Mrk 231 due to reflection. The correction factor of 25, therefore, is a maximum correction factor. The minimum scaling factor is 10 to simply correct for a reflecting surface fraction of 10%. We will conservatively assume this minimum scaling factor of 10 for the reflection component. For the scattering component, we will assume the same scattering fraction as Maloney & Reynolds (2000) (i.e. 1% for electron scattering). After the corrections, the intrinsic 0.2–10 keV luminosity of the AGN in this scenario, where reflection dominates the observed flux, is  $1.4 \times 10^{43}$  ergs s<sup>-1</sup> (from reflection) and  $4.5 \times 10^{43}$  ergs s<sup>-1</sup> (from scattering). Therefore, the total reflection- and scattering-corrected luminosity in the 0.2–10 keV band is  $5.9 \times 10^{43}$  ergs s<sup>-1</sup> if we assume reflected light dominates the observed spectrum.

Similarly, for the second scenario where the majority of the observed flux was scattered into the line of sight, we will assume the reflection component is 25% and the scattering component is 75% of the total observed flux. This implies that the intrinsic 0.2–10 keV luminosity of the AGN is  $4.5 \times 10^{42}$  ergs s<sup>-1</sup> (from reflection) and  $1.4 \times 10^{44}$  ergs s<sup>-1</sup> (from scattering). Hence, the corrected 0.2–10 keV luminosity is  $1.4 \times 10^{44}$  ergs s<sup>-1</sup>. It should be noted that in both cases we considered, the luminosity from the scattering portion dominated the total after the corrections.

Thus, with the assumptions made above, the intrinsic 0.2–10 keV luminosity of the AGN ranges from 0.6 to  $1.4 \times 10^{44}$  ergs s<sup>-1</sup>. This range in luminosity overlaps with that of quasars ( $\sim 10^{44}$  ergs s<sup>-1</sup>; e.g., Elvis et al. 1994; Piconcelli et al. 2005) and is similar to that of NGC 6240 ( $\sim 0.7 - 2 \times 10^{44}$  ergs s<sup>-1</sup>, after correction for an HI column density of  $1 - 2 \times 10^{24}$  cm<sup>-2</sup>; Vignati et al. 1999). The ratio  $\log[L_{2-10 \text{ keV}}/L_{\text{IR}}]$  for F04103–2838 corrected for scattering and reflection is  $-2.2$  to  $-1.7$ . These values fall precisely within the range found in radio-quiet PG quasars ( $-3$  to  $-1$ ; Sanders et al. 1989). Assuming F04103–2838 has the same X-ray to bolometric luminosity ratio as radio-quiet QSOs (Elvis et al. 1994,  $L_x/L_{\text{bol}} \sim 3\%$ ), the AGN contribution to the bolometric luminosity of F04103–2838 is  $\sim 15\text{--}38\%$ . Therefore, within the large uncertainties, the AGN in F04103–2838 does not dominate the total energy output of the galaxy.

## 5. Summary

The results from our analysis of the *XMM-Newton* spectrum of the 1-Jy ULIRG/LINER F04103–2838 can be summarized as follows:

1. The soft (0.2–2 keV) X-ray flux of F04103–2838 is attributed to hot gas with  $kT \sim 0.1$  keV. This temperature is similar to that derived in other starburst galaxies and LINERs. The electron density in F04103–2838 is  $\sim 0.6\text{--}5.9 \text{ cm}^{-3}$ , consistent with theoretical predictions and observational estimates in wind systems.
2. An Fe  $K\alpha$  line located at  $\sim 6.4$  keV with an equivalent width of  $\sim 1.6$  keV is detected in F04103–2838. The line could be intrinsically broad or could be made up of two narrow lines located at rest frame energies of  $\sim 6.3$  and 6.7 keV but this decomposition is only significant at the  $\sim 60\%$  level, so it needs to be verified with higher resolution spectra.
3. The large equivalent width of the Fe  $K\alpha$  line suggests that the AGN is Compton-thick. Using simple assumptions, we estimate that the intrinsic 0.2–10 keV luminosity of this AGN is  $0.6 - 1.4 \times 10^{44} \text{ ergs s}^{-1}$ . If these assumptions are correct and the galaxy has a QSO-like X-ray to bolometric luminosity ratio, the AGN detected by our observations does not dominate the bolometric luminosity of F04103–2838.
4. The X-ray spectral characteristics of F04103–2838 are strikingly similar to those of the local luminous infrared galaxy NGC 6240. Given the similarities in X-ray properties but differences in merger state and in infrared color and luminosity, objects like NGC 6240 could conceivably be the precursors of ULIRGs like F04103–2838.

We are grateful for the referee’s comments and suggestions which helped improve this paper. Thanks are due to Drs. Chris Reynolds, Cole Miller, and Yuxuan Yang for useful discussions. This research is based on observations obtained with *XMM-Newton*, an ESA science mission with instruments and contributions directly funded by ESA Member States and NASA. We made use of the NASA/IPAC Extragalactic Database (NED), which is operated by the Jet Propulsion Laboratory, Caltech, under contract with NASA. We acknowledge support from NASA/*XMM-Newton* Guest Observer Program under grant NNX06AF51G.

## REFERENCES

- Boller, Th., Keil, R., Hasinger, G., Costantini, E., Fujimoto, R., Anabuki, N., Lehmann, I., & Gallo, L. 2003, *A&A*, 411, 63
- Braito, V., Franceschini, A., Della Ceca, R., Severgnini, P., Bassani, L., Cappi, M., Malaguti, G., Palumbo, G.G.C., Persic, M., Risaliti, G., & Salvati, M. 2003, *A&A*, 398, 107
- Braito, V., Della Ceca, R., Piconcelli, E., Severgnini, P., Bassani, L., Cappi, M., Franceschini, A., Iwasawa, K., Malaguti, G., Marziani, P., Palumbo, G.G.C., Persic, M., Risaliti, G., & Salvati, M. 2004, *A&A*, 420, 79
- Bryant, P. M., & Scoville, N. Z. 1999, *AJ*, 117, 2632
- Cecil, G., Bland-Hawthorn, J., & Veilleux, S. 2002, *ApJ*, 576, 745
- Chen, P.S., & Zhang, P. *AJ*, 131, 1942
- Dasyra, K.M. et al. 2006a, *ApJ*, 638, 745
- Dasyra, K.M. et al. 2006b, *ApJ*, 651, 835
- Dasyra, K.M. et al. 2007, *ApJ*, 657, 102
- Dickey & Lockman, 1990, *ARAA*, 28, 215
- Elvis, M., Wilkes, B.J., McDowell, J.C., Green, R.F., Bechtold, J., Willner, S.P., Oey, M.S., Polomski, E., & Cutri, R. 1994, *ApJS*, 95, 1.
- Franceschini, A., Braito, V., Persic, M., Della Ceca, R., Bassani, L., Cappi, M., Malaguti, P., Palumbo, G.G.C., Risaliti, G., Salvati, M., & Severgnini, P. 2003, *MNRAS*, 343, 1181
- González-Martín, O., Masegosa, J., Márquez, I., Guerrero, M.A., & Dultzin-Hacyan, D. 2006, *A&A*, 460, 45
- Gehrels, N. 1986, *ApJ*, 303, 336
- Genzel, R., et al. 1998, *ApJ*, 498, 579
- Ghisellini, G., Harrdt, F., & Matt, G. 1994, *MNRAS*, 267, 743
- Grimes, J.P., Heckman, T., Strickland, D., & Ptak, A., 2005, *ApJ*, 628, 187

- Hopkins, P.F., Hernquist, L., Cox, T.J., Di Matteo, T., Martini, P., Robertson, B., & Springel, V. 2005, *ApJ*, 630, 705
- Ishida, C. M. 2004, PhD Thesis, University of Hawaii
- Imanishi, M., Terashima, Y., Anabuki, N., & Nakagawa, T. 2003, *ApJ*, 596, L167
- Imanishi, M. & Terashima, Y. 2004, *ApJ*, 127, 758
- Iwasawa, K., Fabian, A.C., & Matt, G. 1997, *MNRAS*, 289, 443
- Iwasawa, K., Sanders, D.B., Evans, A.S., Trentham, N., Miniutti, G., & Spoon, H.W.W. 2005, *MNRAS*, 357, 565
- Kim, D.-C., & Sanders, D.B. 1998, *ApJS*, 119, 41
- Kim, D.-C., Veilleux, S., & Sanders, D.B. 1998, *ApJ*, 508, 627
- Kim, D.-C., Veilleux, S., & Sanders, D.B. 2002, *ApJS*, 143, 277
- Kirsch, M., & EPIC Consortium, 2006, XMM-EPIC Status of Calibration and Data Analysis [<http://xmm.vilspa.esa.es/docs/documents/CAL-TN-0018.pdf>]
- Komossa, S., Burwitz, V., Hasinger, G., Predehl, P., Kaastra, J.S., & Ikebe, Y. 2003, *ApJ*, 582, L15
- Krolik, J.H., Madau, P., & Zycki, P.T. 1994, *ApJ*, 420, L57
- Levenson, N.A., Krolik, J.H., Zycki, P.T., Heckman, T.M., Weaver, K.A., Awaki, H., & Terashima, Y. 2002, *ApJ*, 573, L81
- Lutz, D., Veilleux, S., & Genzel, R. 1999, *ApJ*, 517, L13
- Maloney, P.R. & Reynolds, C.S. 2000, *ApJ*, 545, L23
- Netzer, H., Lemze, D., Kaspi, S., George, I.M., Turner, T.J., Lutz, D., Boller, Th., & Chelouche, D. 2005, *ApJ*, 629, 739
- Piconcelli, E., Jimenez-Bailon, E., Guainazzi, M., Schartel, N., Rodriguez-Pascual, P. M., & Santos-Lleo, M. 2005, *A&A*, 432, 15
- Ptak, A., Heckman, T., Levenson, N.A., Weaver, K., & Strickland, D. 2003, *ApJ*, 592, 787
- Rupke, D.S., Veilleux, S., & Sanders, D.B. 2002, *ApJ*, 570, 588

- Rupke, D.S., Veilleux, S., & Sanders, D.B. 2005a, *ApJS*, 160, 87
- Rupke, D.S., Veilleux, S., & Sanders, D.B. 2005b, *ApJS*, 160, 115
- Rupke, D.S., Veilleux, S., & Sanders, D.B. 2005c, *ApJ*, 632, 751
- Rybicki, G.B., & Lightman, A.P., 1979, *Radiative Processes in Astrophysics* (New York Wiley Interscience)
- Sanders, D.B., Phinney, E.S., Neugebauer, G., Soifer, B.T., & Matthews, K. 1989, *ApJ*, 347, 29
- Strickland, D.K. & Stevens, I.R. 2000, *MNRAS*, 314, 511
- Strickland, D.K., Heckman, T. M., Colbert, E. J. M., Hoopes, C. G., & Weaver, K. A. 2004, *ApJ*, 606, 829
- Strickland, D.K., Heckman, T. M., Colbert, E. J. M., Hoopes, C. G., & Weaver, K. A. 2004, *ApJS*, 151, 193
- Surace, J.A., & Sanders, D.B. 1999, *ApJ*, 512, 162
- Taniguchi, Y., Yoshino, A., Ohyama, Y., & Nishiura, S. 1999, *ApJ*, 514, 660
- Teng, S.H., Wilson, A.S., Veilleux, S., Young, A.J., Sanders, D.B., & Nagar, N.M. 2005, *ApJ*, 633, 664 (Paper I)
- Terashima, Y., Iyomoto, N., Ho, L.C., & Ptak, A.F. 2002, *ApJS*, 139, 1
- Veilleux, S., Kim, D.-C., Sanders, D.B., Mazzarella, J.M. & Soifer, B.T., 1995, *ApJS*, 98, 171
- Veilleux, S., Sanders, D.B., & Kim, D.-C. 1997, *ApJ*, 484, 92
- Veilleux, S., Kim, D.-C., & Sanders, D.B. 1999a, *ApJ*, 522, 113
- Veilleux, S., Sanders, D.B., & Kim, D.-C. 1999b, *ApJ*, 522, 139
- Veilleux, S., Kim, D.-C., & Sanders, D.B. 2002, *ApJS*, 143, 315
- Veilleux, S. et al., 2006, *ApJ*, 643, 707
- Vignati, P. et al., 1999, *A&A*, 349, L57



Table 1. Best-fit Parameters to Models A, B, & C<sup>†</sup>

Model	A	A	A	A	B	B	B	B	C
Parameters	15 cts bin <sup>-1</sup>	5 cts bin <sup>-1</sup>	3 cts bin <sup>-1</sup>	unbinned	15 cts bin <sup>-1</sup>	5 cts bin <sup>-1</sup>	3 cts bin <sup>-1</sup>	unbinned	unbinned
N <sub>H</sub> <sup>a</sup>	0.20 <sup>+0.28</sup> <sub>-0.16</sub>	0.00 <sup>+0.04</sup> <sub>-0.00</sub>	0.00 <sup>+0.04</sup> <sub>-0.00</sub>	0.00 <sup>+0.04</sup> <sub>-0.00</sub>	0.30 <sup>+0.36</sup> <sub>-0.22</sub>	0.00 <sup>+0.06</sup> <sub>-0.00</sub>	0.00 <sup>+0.06</sup> <sub>-0.00</sub>	0.00 <sup>+0.06</sup> <sub>-0.00</sub>	0.19 <sup>+0.33</sup> <sub>-0.19</sub>
Γ	1.42 <sup>+0.61</sup> <sub>-0.41</sub>	1.01 <sup>+0.21</sup> <sub>-0.20</sub>	1.00 <sup>+0.21</sup> <sub>-0.20</sub>	1.00 <sup>+0.21</sup> <sub>-0.20</sub>	1.80 <sup>+0.90</sup> <sub>-0.60</sub>	1.12 <sup>+0.25</sup> <sub>-0.22</sub>	1.11 <sup>+0.26</sup> <sub>-0.22</sub>	1.09 <sup>+0.27</sup> <sub>-0.22</sub>	1.36 <sup>+0.97</sup> <sub>-0.44</sub>
E <sub>line</sub> <sup>b</sup>	—	—	—	—	6.57 <sup>+1.46</sup> <sub>-1.20</sub>	6.37 <sup>+0.18</sup> <sub>-0.17</sub>	6.42 <sup>+0.26</sup> <sub>-0.29</sub>	6.43 <sup>+0.27</sup> <sub>-0.28</sub>	6.43 <sup>+0.26</sup> <sub>-0.26</sub>
σ <sup>b</sup>	—	—	—	—	0.00 <sup>+1.20</sup> <sub>-0.00</sub>	0.14 <sup>+0.20</sup> <sub>-0.14</sub>	0.23 <sup>+0.28</sup> <sub>-0.23</sub>	0.25 <sup>+0.25</sup> <sub>-0.25</sub>	0.26 <sup>+0.24</sup> <sub>-0.26</sub>
EW <sup>b</sup>	—	—	—	—	1.96 <sup>+19.54</sup> <sub>-1.95</sub>	1.33 <sup>+1.24</sup> <sub>-0.89</sub>	1.37 <sup>+1.38</sup> <sub>-1.01</sub>	1.39 <sup>+1.37</sup> <sub>-1.02</sub>	1.62 <sup>+1.58</sup> <sub>-1.12</sub>
kT <sup>b</sup>	—	—	—	—	—	—	—	—	0.10 <sup>+0.03</sup> <sub>-0.08</sub>
Stat./dof <sup>c</sup>	12.4/11	66.5/40	83.0/67	858.2/1958	8.6/8	58.8/37	77.1/64	852.1/1955	848.1/1953
F <sub>0.2–2keV</sub> (total) <sup>d</sup>	0.96 <sup>+0.42</sup> <sub>-0.71</sub>	1.07 <sup>+0.29</sup> <sub>-0.21</sub>	1.07 <sup>+0.29</sup> <sub>-0.21</sub>	1.05 <sup>+0.30</sup> <sub>-0.20</sub>	2.93 <sup>+0.68</sup> <sub>-1.40</sub>	1.08 <sup>+0.17</sup> <sub>-0.19</sub>	1.08 <sup>+0.21</sup> <sub>-0.19</sub>	1.06 <sup>+0.19</sup> <sub>-0.21</sub>	2.17 <sup>+0.87</sup> <sub>-0.87</sub>
(AGN) <sup>d</sup>	—	—	—	—	2.93 <sup>+0.68</sup> <sub>-1.40</sub>	1.08 <sup>+0.17</sup> <sub>-0.19</sub>	1.08 <sup>+0.21</sup> <sub>-0.19</sub>	1.06 <sup>+0.19</sup> <sub>-0.21</sub>	1.64 <sup>+0.86</sup> <sub>-0.50</sub>
F <sub>2–10keV</sub> (total) <sup>d</sup>	3.96 <sup>+1.37</sup> <sub>-2.57</sub>	4.70 <sup>+3.58</sup> <sub>-2.04</sub>	4.73 <sup>+3.62</sup> <sub>-2.12</sub>	4.85 <sup>+3.75</sup> <sub>-2.10</sub>	3.65 <sup>+1.64</sup> <sub>-1.02</sub>	4.57 <sup>+2.27</sup> <sub>-3.05</sub>	4.60 <sup>+1.54</sup> <sub>-3.27</sub>	4.76 <sup>+3.35</sup> <sub>-2.75</sub>	4.56 <sup>+2.04</sup> <sub>-0.98</sub>
(AGN) <sup>d</sup>	—	—	—	—	3.65 <sup>+1.64</sup> <sub>-1.02</sub>	4.57 <sup>+2.27</sup> <sub>-3.05</sub>	4.60 <sup>+1.54</sup> <sub>-3.27</sub>	4.76 <sup>+3.35</sup> <sub>-2.75</sub>	4.56 <sup>+1.92</sup> <sub>-1.01</sub>
L <sub>0.2–2keV</sub> (total) <sup>e</sup>	0.29 <sup>+0.12</sup> <sub>-0.21</sub>	0.31 <sup>+0.09</sup> <sub>-0.06</sub>	0.31 <sup>+0.09</sup> <sub>-0.06</sub>	0.31 <sup>+0.09</sup> <sub>-0.06</sub>	0.86 <sup>+0.20</sup> <sub>-0.41</sub>	0.31 <sup>+0.05</sup> <sub>-0.06</sub>	0.31 <sup>+0.06</sup> <sub>-0.05</sub>	0.31 <sup>+0.05</sup> <sub>-0.06</sub>	0.64 <sup>+0.26</sup> <sub>-0.26</sub>
(AGN) <sup>e</sup>	—	—	—	—	0.86 <sup>+0.20</sup> <sub>-0.41</sub>	0.31 <sup>+0.05</sup> <sub>-0.06</sub>	0.31 <sup>+0.06</sup> <sub>-0.05</sub>	0.31 <sup>+0.05</sup> <sub>-0.06</sub>	0.48 <sup>+0.26</sup> <sub>-0.15</sub>
L <sub>2–10keV</sub> (total) <sup>e</sup>	1.16 <sup>+0.40</sup> <sub>-0.76</sub>	1.39 <sup>+1.06</sup> <sub>-0.60</sub>	1.40 <sup>+1.06</sup> <sub>-0.62</sub>	1.44 <sup>+1.11</sup> <sub>-0.62</sub>	1.07 <sup>+0.45</sup> <sub>-0.30</sub>	1.35 <sup>+0.67</sup> <sub>-0.90</sub>	1.36 <sup>+0.45</sup> <sub>-0.96</sub>	1.40 <sup>+0.99</sup> <sub>-0.81</sub>	1.35 <sup>+0.50</sup> <sub>-0.29</sub>
(AGN) <sup>e</sup>	—	—	—	—	1.07 <sup>+0.49</sup> <sub>-0.30</sub>	1.35 <sup>+0.67</sup> <sub>-0.90</sub>	1.36 <sup>+0.45</sup> <sub>-0.96</sub>	1.40 <sup>+0.99</sup> <sub>-0.81</sub>	1.35 <sup>+0.57</sup> <sub>-0.30</sub>

<sup>†</sup>Model A: Absorption<sub>Galactic</sub> × Absorption<sub>source</sub> × PL. Model B: Absorption<sub>Galactic</sub> × Absorption<sub>source</sub> × (PL + Line). Model C: Absorption<sub>Galactic</sub> × [MEKAL + Absorption<sub>source</sub> × (PL + Line)], where MEKAL is the Mewe, Kaastra, & Liedahl thermal plasma model (see the XSPEC manual for details), PL is a power-law model representing the AGN, Line is the Fe K emission line with a Gaussian profile, Absorption<sub>Galactic</sub> is the absorption from N<sub>H,Galactic</sub> = 2.45 × 10<sup>20</sup> atoms cm<sup>-2</sup>, and Absorption<sub>source</sub> is the intrinsic absorption within the source.

<sup>a</sup>Intrinsic (i.e. within the galaxy) column density in units of 10<sup>22</sup> atoms cm<sup>-2</sup>.

<sup>b</sup>Fe K line energy (rest frame), width, equivalent width, and thermal gas temperature all in keV.

<sup>c</sup>Fitting statistics per degrees of freedom. Cash statistics are used for unbinned spectra and spectra binned to at least 3 and 5 counts bin<sup>-1</sup>, while χ<sup>2</sup> statistics are used for spectra binned to at least 15 counts bin<sup>-1</sup>.

<sup>d</sup>Absorption-corrected flux in units of 10<sup>-14</sup> ergs cm<sup>-2</sup> s<sup>-1</sup>. The AGN value includes the flux from both the power-law component and the iron line.

<sup>e</sup>Absorption-corrected luminosity in units of  $10^{42}$  ergs  $s^{-1}$ . The AGN value includes the flux from both the power-law component and the iron line.

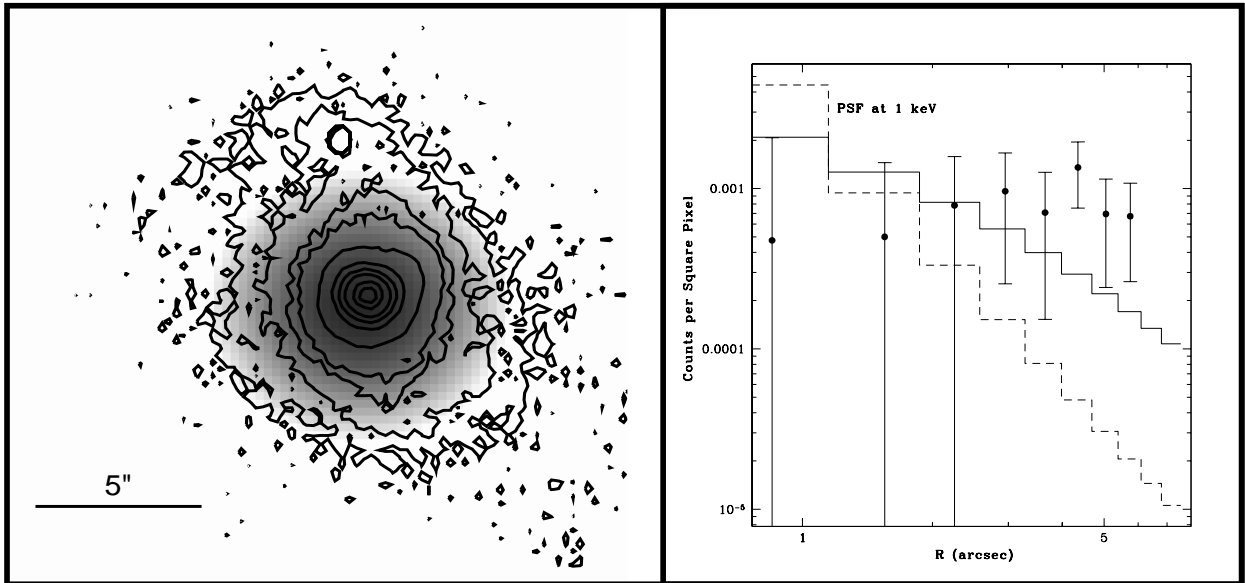


Fig. 1.— *Left*: EPIC mosaic image of F04103–2838 smoothed with a Gaussian ( $\text{FWHM} \sim 5''$ ) and displayed on a linear grey scale. The contours are optical R-band data from Kim et al. (2002). *Right*: Comparison of unsmoothed EPIC PN PSF at 1 keV with observed 0.2–2 keV radial profile of F04103–2838. The dashed line represents the theoretical PSF while the solid line represents the PSF broadened due to uncertainties in the correction for pointing drift of the telescope. The absolute pointing drift (APD) error is conservatively assumed to be  $3''$ , the upper limit (see *XMM-Newton* Observer’s Handbook). The error bars were calculated using Gehrels (1986). The source is unresolved within the uncertainty of the measurements.

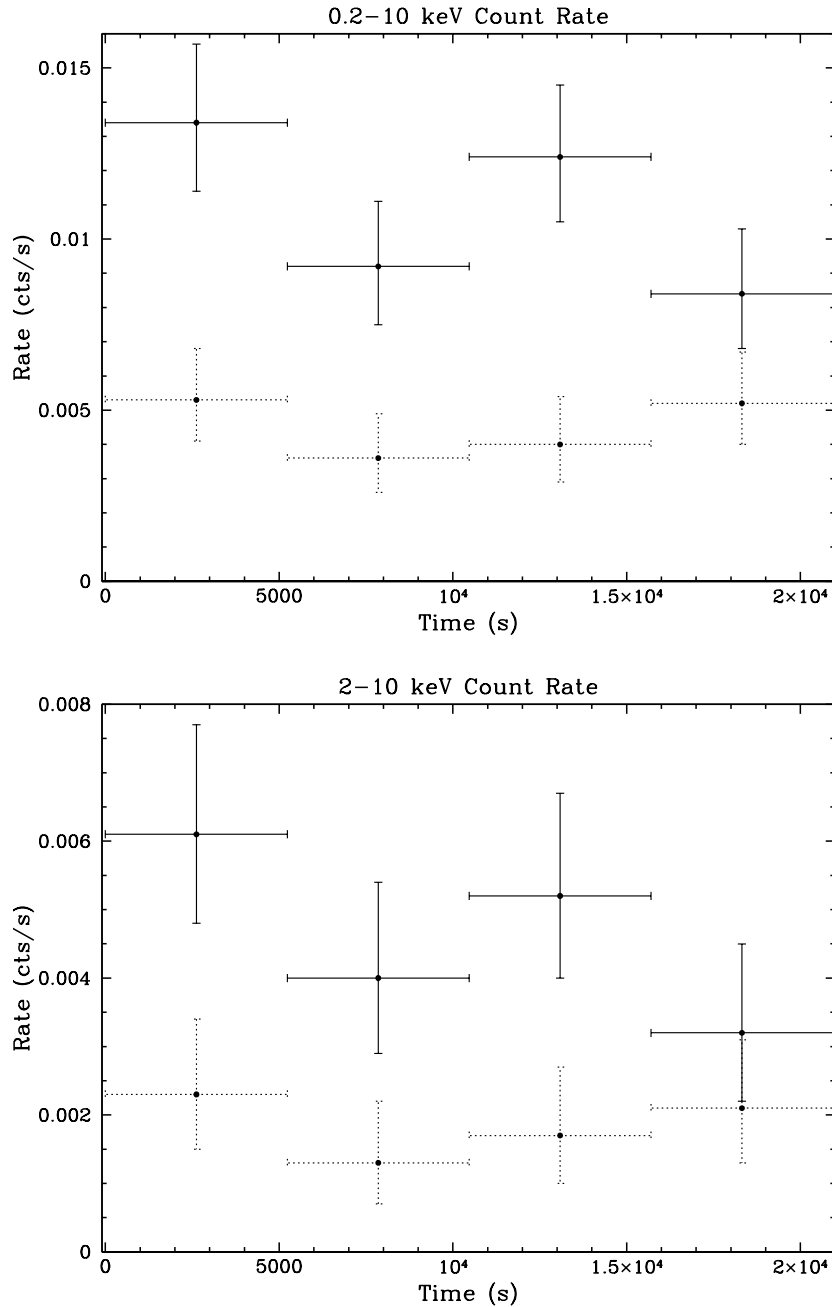


Fig. 2.— The 0.2–10 keV and 2–10 keV light curves for F04103–2838. The solid crosses denote the source count rate, while the dotted crosses denote the background count rate. Background-subtraction was not applied to the source spectrum. The time bins are each 5234 seconds. The error bars are Poissonian counting errors calculated following Gehrels (1986) at the 84% significance level. Within the errors, the source is not variable on the  $\sim 20$  ksec time scale of our observation. The lack of short timescale variations is expected of sources where most of the primary X-ray flux is absorbed or reprocessed.

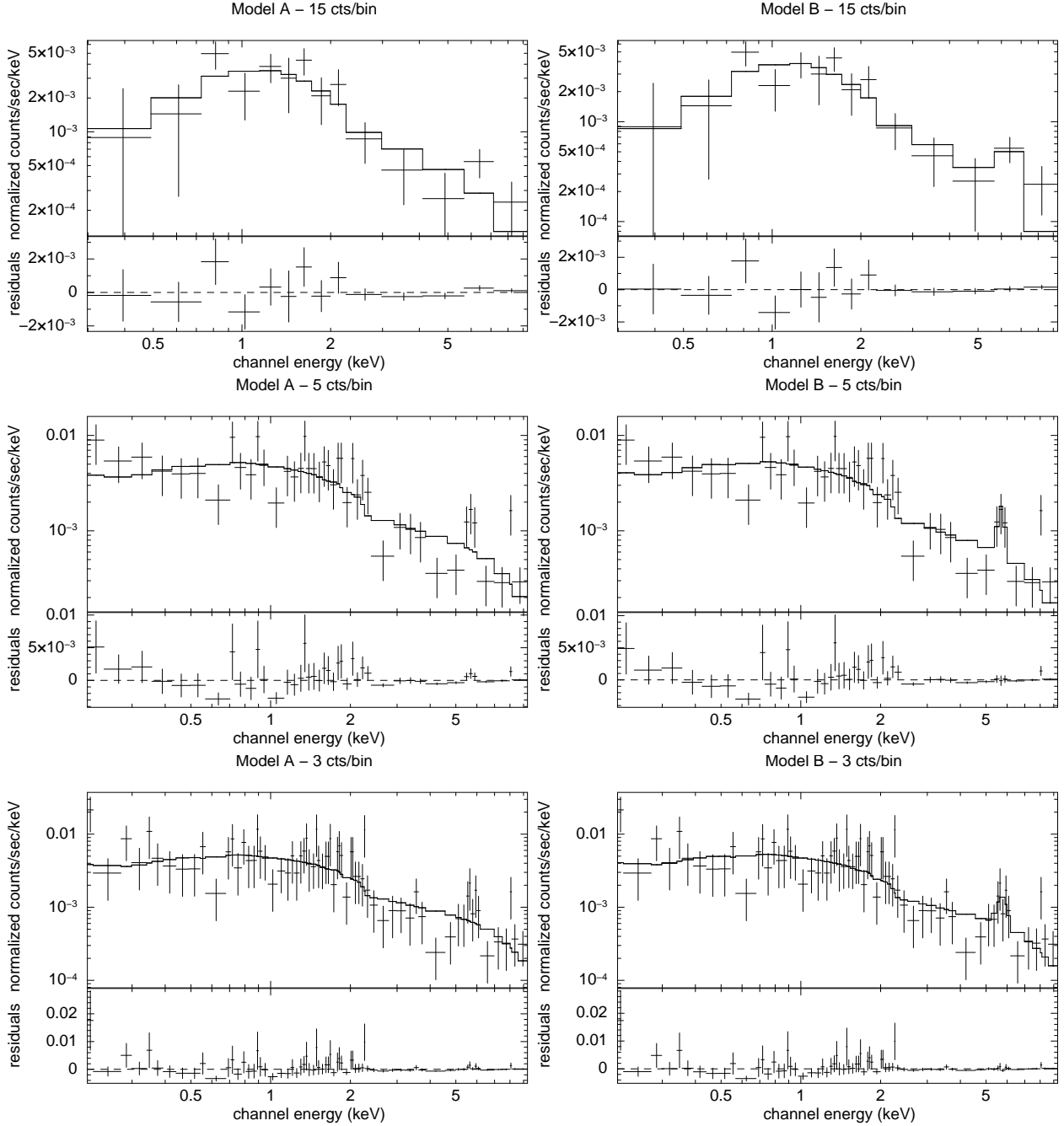


Fig. 3.— EPIC PN spectrum and best-fit models to F04103–2838 with different binnings:  $\geq 15$  counts  $\text{bin}^{-1}$  (top panels),  $\geq 5$  counts  $\text{bin}^{-1}$  (middle), and  $\geq 3$  counts  $\text{bin}^{-1}$  (bottom). The unbinned spectrum was modeled but is not shown here. Model A (left panels) is a simple absorbed power-law distribution; model B (right) is the same as A, but includes a Gaussian component to model the Fe K emission. The best-fit model parameters are listed in Table 1. The iron line is most prominent in the data binned to 5 counts  $\text{bin}^{-1}$  and the Fe K doublet may be present in the 3 counts  $\text{bin}^{-1}$  data. X-axis of the figures represents energy in the observer’s frame.

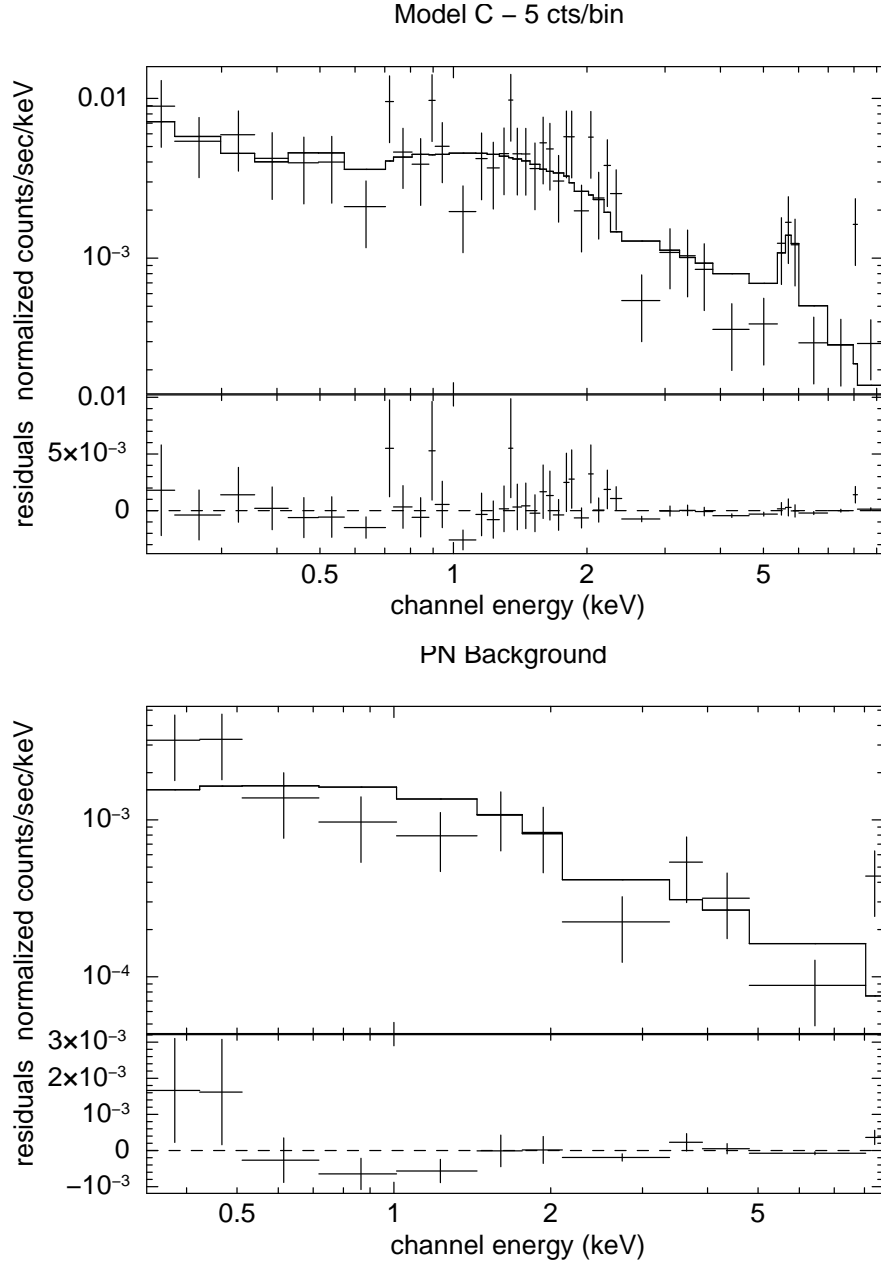


Fig. 4.— EPIC PN source and background spectra of F04103–2838 binned to at least 5 counts  $\text{bin}^{-1}$  with the best-fit *unbinned* model (C) applied. The X-axis of the figures represents energy in the observer’s frame. *Top*: The source model includes a MEKAL component for the thermal emission, a power-law component to represent the AGN component, a Gaussian component to model the Fe K emission, and a relatively flat power-law ( $\Gamma \sim 1.0$ ) for the background. The model parameters are listed in Table 1. *Bottom*: A binned background spectrum with the background model used in the modeling of the unbinned spectrum and spectra binned to at least 5 and 3 counts  $\text{bin}^{-1}$ . No significant features are seen in the background spectrum.

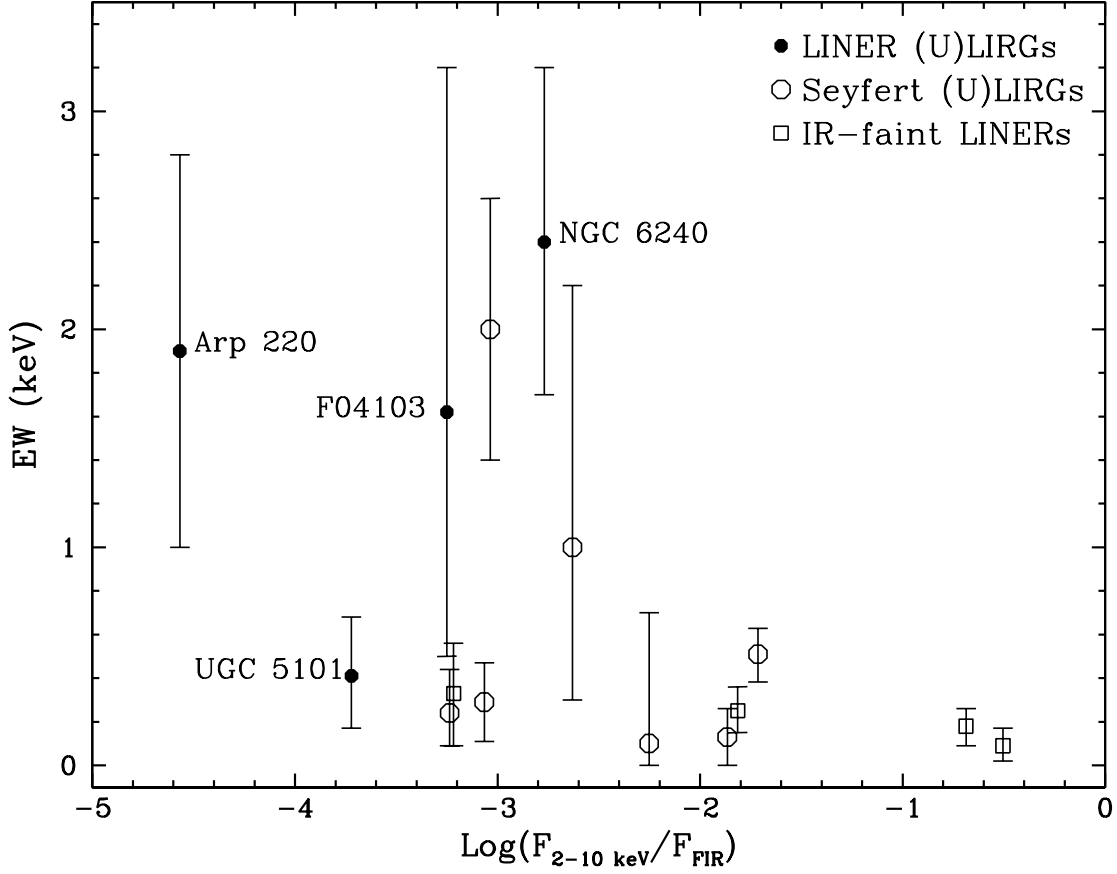


Fig. 5.— Distribution of equivalent widths of Fe K emission features in LINERs and (U)LIRGs versus absorption-corrected 2–10 keV to far-infrared flux ratio. In general, the (U)LIRGs have higher EWs than IR-faint LINERs. Of these, F19254–7245 (EW $\sim$ 2 keV) was determined to be Compton-thick by Braito et al. (2003). The values included in this figure are drawn from Terashima et al. (2002), Braito et al. (2003), Imanishi et al. (2003), Ptak et al. (2003), Braito et al. (2004), Imanishi & Terashima (2004), Iwasawa et al. (2005), Paper I, and this work. The equivalent widths for the four LINER (U)LIRGs included in this sample are labeled. The F04103–2838 value plotted is derived from our best-fit model (C). Note that Komossa et al. (2003) detected Fe K emission from each of the two nuclei in NGC 6240. Therefore, the single value quoted by Ptak et al. (2003) is a sum of the Fe K $\alpha$  and Fe K $\beta$  emission due to neutral iron, likely dominated by the brighter southern nucleus. The value quoted for Arp 220 may also be due to a blend of emission lines arising from ionized iron (Fe XX up to Fe XXVI). The value ( $\sim$ 0.5 keV) quoted for the ULIRG Mrk 463 is a sum of the emission due to neutral iron and Fe XXV.